

# Accretion in Binary Systems with Slow Stellar Winds

Jesús A. Toalá<sup>1</sup>, Emilio Tejeda<sup>2</sup> and Diego A. Vasquez-Torres<sup>1</sup>

<sup>1</sup>Instituto de Radioastronomía y Astrofísica, Universidad Nacional Autónoma de México, Morelia 58089, México

<sup>2</sup>SECIHTI-Instituto de Física y Matemáticas, Universidad Michoacana de San Nicolás de Hidalgo, Ciudad Universitaria, 58040 Morelia, Mich., Mexico

**Keywords:** accretion, accretion discs — (stars:) binaries: symbiotic — stars: low-mass stars — stars: winds, outflows — stars: AGB and post-AGB

## Abstract

Wind accretion in binary systems is commonly described using the Bondi–Hoyle–Lyttleton (BHL) formalism. However, its standard implementation fails in the slow-wind regime, where the wind velocity of the donor star ( $v_w$ ) is comparable to or smaller than the orbital velocity of the accretor ( $v_o$ ). Tejeda & Toalá recently proposed a geometrical correction to the BHL formalism that accounts for the wind aberration caused by the binary’s orbital motion, which tilts the accretion cylinder and reduces its effective cross-section. Here we present a suite of smoothed particle hydrodynamic simulations performed with PHANTOM to test wind accretion in binary systems operating in this slow-wind regime. We explore circular configurations and directly measure mass accretion efficiencies from the simulations. Our results confirm that the standard BHL prescription systematically overestimates accretion rates for  $v_w/v_o < 1$ , while the geometrically corrected model reproduces the simulated efficiencies with remarkable accuracy. A key finding is that the velocity relevant for accretion estimates is not the value derived from the unperturbed stellar wind, but the local gas velocity measured upstream of the accretor. The gravitational potential of the accretor perturbs the flow, altering the effective relative velocity and modifying the accretion efficiency, particularly for compact orbits. These results provide strong numerical support for the geometrically corrected framework and establish a physically motivated basis for modeling wind-fed accretion in interacting binaries, including symbiotic systems.

## Resumen

La acreción por viento en sistemas binarios se describe comúnmente mediante el formalismo de Bondi–Hoyle–Lyttleton (BHL). Sin embargo, su implementación estándar falla en el régimen de vientos lentos, donde la velocidad del viento de la estrella donadora ( $v_w$ ) es comparable o menor que la velocidad orbital del acretor ( $v_o$ ). Tejeda & Toalá recientemente propusieron una corrección geométrica al formalismo BHL que representa la aberración del viento causada por el movimiento orbital de la binaria, la cual inclina el cilindro de acreción y reduce su sección eficaz efectiva. Aquí presentamos un conjunto de simulaciones hidrodinámicas de partículas suavizadas realizadas con PHANTOM para estudiar la acreción por viento en sistemas binarios que operan en dicho régimen. Exploramos configuraciones circulares y medimos directamente las eficiencias de acreción de masa a partir de las simulaciones. Nuestros resultados confirman que la prescripción estándar de BHL sobrestima sistemáticamente las tasas de acreción para  $v_w/v_o < 1$ , mientras que el modelo geométricamente corregido reproduce las eficiencias obtenidas en las simulaciones con excelente precisión. Un resultado clave es que la velocidad relevante para estimar la acreción no es la del viento estelar no perturbado, sino la velocidad local del gas medida corriente arriba en las inmediaciones del acretor. El potencial gravitacional del acretor perturba el flujo, alterando la velocidad relativa efectiva y modificando la eficiencia de acreción, particularmente en órbitas compactas. Estos resultados proporcionan un fuerte respaldo numérico al marco de acreción geométricamente corregido y establecen una base físicamente motivada para modelar la acreción alimentada por viento en binarias interactuantes, incluyendo sistemas simbióticos.

**Corresponding author:** Jesús A. Toalá *E-mail address:* j.toala@irya.unam.mx

**Received:** March 3, 2026

## 1. Introduction

Our understanding of wind accretion in binary systems has been built upon the classic Bondi–Hoyle–Lyttleton (BHL) scheme (Hoyle & Lyttleton, 1939; Bondi & Hoyle, 1944). Originally developed to describe a point mass accretor moving supersonically along a straight-line trajectory through a uniform medium, the BHL model found one of its earliest binary applications in the work of Davidson & Ostriker (1973), who used it to investigate the X-ray properties of high-mass X-ray binaries (HMXBs) such as Cen X-3 and Her X-1. Since those seminal studies, the BHL

framework has become a fundamental tool for modeling wind-fed accretion in HMXBs (e.g., Shakura et al., 2015; Weng & Ji, 2024, and references therein).

The BHL framework has also been widely applied to study symbiotic systems, where a white dwarf (WD) accretes material from the stellar wind of a late-type companion, typically a red giant or an asymptotic giant branch (AGB) star (Mikołajewska, 2003; Merc, 2025). However, this application has met with significantly less success (Boffin, 2015). Several studies have shown that for these configurations, the standard BHL prescription consistently

and significantly overestimates the resulting mass accretion rate compared to numerical simulations (Theuns et al., 1996; Nagae et al., 2004; Saladino et al., 2019). In certain cases, the model even yields non-physical results where the predicted mass accretion efficiency exceeds unity.

The applicability of the BHL formalism in a binary context depends primarily on the relative velocity between the accretor and the donor’s stellar wind. This relationship is characterized by the dimensionless velocity parameter

$$w = \frac{v_w}{v_o}, \quad (1)$$

where  $v_w$  is the wind velocity at the position of the accretor and  $v_o$  is the orbital velocity, with typical values of  $v_o \approx 5\text{--}50 \text{ km s}^{-1}$ . The direct implementation of the BHL model has proven highly successful for systems where  $w > 1$ , a condition commonly met in HMXBs where the winds of the donor stars are often at least one order of magnitude larger than the orbital velocities (see, e.g., Hainich et al., 2020, and references therein).

In contrast, symbiotic systems typically operate in the slow-wind regime ( $w \lesssim 1$ ), where the donor’s wind velocity is comparable to or smaller than the orbital velocity of the accretor. These systems feature low-velocity winds, with observed values in the range of  $v_w \approx 5\text{--}20 \text{ km s}^{-1}$  (Ramstedt et al., 2020; Wallström et al., 2025). It is in this  $w \lesssim 1$  regime where the standard BHL prescription systematically overestimates mass accretion rates.

To address the limitations of the standard BHL scheme in binary systems with low-velocity winds, an alternative mechanism known as Wind Roche Lobe Overflow (WRLO) was proposed in Mohamed & Podsiadlowski (2007) and Podsiadlowski & Mohamed (2007). The WRLO scenario occurs when the wind injection radius of the mass-losing star is comparable to its Roche Lobe radius ( $r_{\text{RL}}$ ), causing the material to be channeled toward the companion through the first Lagrangian point. However, Mohamed & Podsiadlowski (2012) later showed that if the wind injection radius remains smaller than  $r_{\text{RL}}$ , the wind accretion regime is recovered regardless of whether the  $w < 1$  condition is met.

Other attempts to mitigate the discrepancies of the BHL model in the slow-wind regime have often relied on *ad hoc* efficiency parameters,  $\alpha_{\text{BHL}}$ , typically ranging from 0.5 to 0.8 (e.g., Saladino & Pols, 2019; Lee et al., 2022; Malfait et al., 2024), without strong physical justification. Alternatively, some studies circumvent these limitations by restricting their analysis to symbiotic systems where  $w > 1$  (e.g., Vathachira et al., 2026).

A recent re-evaluation of the standard wind accretion model applied to binaries was presented by Tejada & Toalá (2025). In that work, our group demonstrated that introducing a simple geometrical correction to the standard BHL formulation is sufficient to alleviate the long-standing discrepancies found in systems operating in the slow-wind regime. This approach accounts for the fact that the stellar wind meets the accretor at a specific angle relative to its orbital motion, modifying the effective cross-section of the accretion cylinder. This new prescription predicts reduced accretion efficiencies for  $w < 1$ , which are better aligned with numerical results, while recovering the standard BHL result for  $w \gg 1$ .

The geometrically corrected framework of Tejada & Toalá (2025) has already been applied to investigate specific objects, such as the symbiotic system R Aquarii (Vasquez-Torres et al., 2024), and to model the long-term evolution of both interacting binaries (Maldonado et al., 2025a,b) and planetary systems (Padilla-López

et al., submitted). Despite this progress, direct comparisons between this analytical prescription and the numerical results available in the literature remain challenging. A primary difficulty lies in the inconsistent wind velocity profiles adopted across different studies, which complicates the benchmarking of accretion models. Moreover, the gravitational potential of the binary interaction substantially modifies the wind velocity experienced by the accretor relative to the unperturbed stellar wind. This effect is further complicated if the accretor is located within the wind acceleration zone of the primary star.

In this paper, we address these challenges by presenting a suite of hydrodynamical simulations to test wind accretion specifically in the slow-wind regime ( $w < 1$ ). We explore various circular configurations to directly measure local gas velocities and mass accretion efficiencies. These results are then compared with the predictions of both the standard BHL model and the geometrically corrected framework of Tejada & Toalá (2025).

The remainder of this article is organized as follows: Section 2 introduces the main model parameters. Section 3 details the numerical setup of our hydrodynamical simulations. Section 4 presents the simulation results, which are subsequently discussed in Section 5. Finally, we summarize our primary findings in Section 6.

## 2. Model description

We consider a binary system consisting of a donor star with mass  $m_1$  and an accreting companion with mass  $m_2$ . The system is characterized by its orbital separation  $a$  and a circular orbit with an orbital velocity  $v_o$  given by

$$v_o = \sqrt{\frac{G(m_1 + m_2)}{a}}. \quad (2)$$

The mass transfer process is governed by the interaction between the donor’s stellar wind, moving at velocity  $v_w$  at the accretor’s position, and the orbital motion of the secondary. This relationship is quantified by the dimensionless velocity parameter  $w$  introduced in Equation (1) and the dimensionless mass ratio  $q$ ,

$$q = \frac{m_2}{m_1 + m_2}. \quad (3)$$

The primary metric of our study is the mass accretion efficiency  $\eta$ , defined as

$$\eta = \frac{\dot{M}_{\text{acc}}}{\dot{M}_w}, \quad (4)$$

where  $\dot{M}_{\text{acc}}$  is the mass accretion rate onto the secondary and  $\dot{M}_w$  the total mass-loss rate of the donor. We compare our numerical results ( $\eta_{\text{sim}}$ ) against two analytical models:

1. **Standard BHL** ( $\eta_{\text{BHL}}$ ). The direct implementation of the BHL model to binary systems leads to

$$\eta_{\text{BHL}} = \frac{q^2}{w(1 + w^2)^{3/2}}, \quad (5)$$

2. **Geometrically corrected model** ( $\eta_{\text{TT}}$ ). The formulation by Tejada & Toalá (2025), which accounts for the effective cross-section of the accretion cylinder by considering the non-zero angle between the wind and the orbital motion

$$\eta_{\text{TT}} = \left( \frac{q}{1 + w^2} \right)^2. \quad (6)$$

The complex hydrodynamical structures arising from these interactions have been extensively documented in numerous numerical studies (see, e.g., Theuns et al., 1996; Nagae et al., 2004; de Val-Borro et al., 2009; Huarte-Espinosa et al., 2013; Liu et al., 2017; Saladino et al., 2019; Saladino & Pols, 2019; Lee et al., 2022; Malfait et al., 2024). They clearly show the formation of a prominent accretion disc around the secondary and a spiral-shaped accretion wake that characterizes wind-fed accretion in the slow-wind regime.

Such works highlight the need for a robust numerical approach to accurately capture the flow dynamics near the accretor. To achieve this, we employ three-dimensional hydrodynamical simulations to bridge the gap between the simplified analytical frameworks and the distorted velocity fields observed in our modeled systems.

### 3. Simulations

We performed three-dimensional smoothed particle hydrodynamic (SPH) simulations using the PHANTOM code (Price et al., 2018).<sup>1</sup> The simulations adopt an adiabatic equation of state of the form

$$P = (\gamma - 1)\rho u, \quad (7)$$

where  $P$  is the gas pressure,  $\rho$  is the volumetric density,  $u$  is the internal energy, and  $\gamma$  is the polytropic index. The temperature of the gas is calculated by adopting the ideal gas equation

$$T = \frac{\mu m_H P}{k_B \rho}, \quad (8)$$

where  $\mu$  is the mean molecular weight,  $m_H$  is the hydrogen mass, and  $k_B$  is the Boltzmann's constant. Constant values for the polytropic index and the mean molecular weight are adopted as  $\gamma = 1.2$  and  $\mu = 1.26$ , the latter being consistent with an atomic wind in AGB stars (Millar, 2004). Our simulations include H I cooling following the methodology presented by Malfait et al. (2024), where the cooling is calculated using the equation (see Spitzer, 1978)

$$\Lambda_{\text{HI}} = 7.3 \times 10^{-19} \frac{n_e n_H e^{-118400/T}}{\rho} \text{ erg cm}^3 \text{ s}^{-1}, \quad (9)$$

with  $n_e$  and  $n_H$  representing the number density of electrons and hydrogen, respectively. The binary simulations were performed adopting the wind routines predefined in PHANTOM and described in Siess et al. (2022).

Our modeled systems are designed to reflect the observable properties of known symbiotic systems (see Appendix A). To explore the parameter space, we performed twenty SPH simulations divided into two distinct families, labeled A and B, based on the dimensionless mass ratio  $q$ :

- **Family A** (Simulations A1-A10): This set adopts a donor mass of  $m_1 = 1.5 M_\odot$  and an accreting companion of  $m_2 = 0.6 M_\odot$ . These masses yield a fixed dimensionless mass ratio of  $q \simeq 0.29$ . We explored ten different orbital separations ranging from 3 to 50 AU.
- **Family B** (Simulations B1-B10): This set adopts a donor mass of  $m_1 = 1.7 M_\odot$  and an accreting companion of  $m_2 = 0.3 M_\odot$ . These masses yield a fixed dimensionless mass ratio of  $q = 0.15$ . We performed ten simulations with orbital separations ranging from 2.5 to 40 AU.

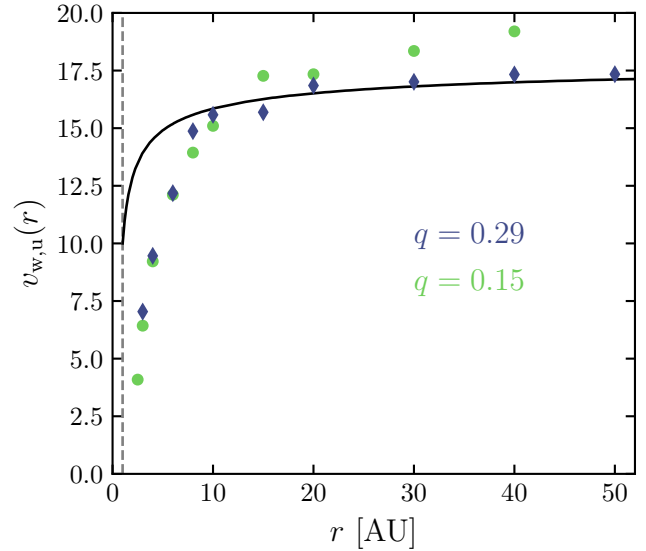


**Figure 1.** Unperturbed wind velocity profile ( $v_{w,u}$ ) for the mass-losing donor star ( $m_1$ ) computed by PHANTOM (solid line). This profile remains identical across all simulations in our suite. The wind is launched from the donor surface with an initial velocity  $v_{\text{ini}} = 10 \text{ km s}^{-1}$ , reaching a terminal speed of  $v_\infty \lesssim 17.8 \text{ km s}^{-1}$ . The dashed vertical line at  $r = 1 \text{ AU}$  indicates the wind injection radius ( $R_1$ ). Symbols represent the local wind velocity ( $v_w$ ) measured upstream near the accretor for each individual simulation.

In both families, the donor star properties are approximated to standard values for an AGB star, with a luminosity of  $L_1 = 5315 L_\odot$  and a radius of  $R_1 = 214 R_\odot (\approx 1 \text{ AU})$ . The secondary is modeled as a sink particle with an accretion radius of 0.01 AU. The stellar wind is modeled by injecting SPH particles at a radial distance  $r = R_1$  from the donor's center, using a constant initial launching velocity of  $v_{\text{ini}} = 10 \text{ km s}^{-1}$ . The resolution parameter (`iwind_res`) is set to 8, which results in an average of  $5 \times 10^5$  particles in the wind. The unperturbed wind velocity profile of the mass donor star computed by PHANTOM is presented as a solid line in Fig. 1, which has a terminal wind velocity of  $v_\infty \lesssim 17.8 \text{ km s}^{-1}$ .

For each of our simulations, we allow the system to evolve until a steady state is reached, characterized by a stable mass accretion rate. We then extract the local wind velocity ( $v_w$ ) and the resulting mass accretion efficiency ( $\eta_{\text{sim}}$ ) by taking a time average over one full binary orbit to minimize numerical noise. The specific physical parameters and the resulting values for each individual run are summarized in Table 1.

Finally, it is important to highlight here that our simulations are meant to explore the slow wind regime without entering the WRLO accretion regime. To confirm this, we calculate the Roche lobe radius ( $r_{\text{RL}}$ ) around the donor star, as listed in the 6th column of Table 1. The table shows that in all cases,  $r_{\text{RL}} > R_1$ , ensuring that we are modeling strictly wind accretion cases.

### 4. Results

In agreement with previous numerical studies of wind accretion in the slow-wind regime, our simulations result in the formation of accretion discs and spiral-shaped wakes around the secondary (see, for example, de Val-Borro et al., 2009; Huarte-Espinosa et al., 2013; Lee et al., 2022; Malfait et al., 2024; Nagae et al., 2004;

<sup>1</sup><https://phantomsp.github.io/>

**Table 1.** Details of circular simulations analyzed in this paper. Note that  $v_w$  is the measured relative velocity of the gas with respect to the accretor, which is used to estimate  $w$ ,  $\eta_{\text{TT}}$ , and  $\eta_{\text{BHL}}$ .

$m_1$	$m_2$	$q$	Label	$a$ (AU)	$r_{\text{RL}}$ (AU)	$v_o$ (km s $^{-1}$ )	$v_w$ (km s $^{-1}$ )	$w$	$\eta_{\text{sim}}$	$\eta_{\text{TT}}$	$\eta_{\text{BHL}}$
1.5	0.6	0.29	A1	3.0	1.38	25.03	7.04	0.281	$6.21 \times 10^{-2}$	$7.21 \times 10^{-2}$	$2.59 \times 10^{-1}$
			A2	4.0	1.84	21.68	9.46	0.437	$5.00 \times 10^{-2}$	$5.76 \times 10^{-2}$	$1.44 \times 10^{-1}$
			A3	6.0	2.76	17.70	11.79	0.666	$3.31 \times 10^{-2}$	$3.91 \times 10^{-2}$	$7.06 \times 10^{-2}$
			A4	8.0	3.68	15.58	14.87	0.954	$2.00 \times 10^{-2}$	$2.22 \times 10^{-2}$	$3.24 \times 10^{-2}$
			A5	10.0	4.60	15.50	15.13	0.976	$1.85 \times 10^{-2}$	$2.14 \times 10^{-2}$	$3.07 \times 10^{-2}$
			A6	15.0	6.90	11.19	15.35	1.372	$0.89 \times 10^{-2}$	$0.98 \times 10^{-2}$	$1.21 \times 10^{-2}$
			A7	20.0	9.17	9.70	17.03	1.755	$0.52 \times 10^{-2}$	$0.49 \times 10^{-2}$	$0.56 \times 10^{-2}$
			A8	30.0	13.79	7.92	17.01	2.147	$2.50 \times 10^{-3}$	$2.59 \times 10^{-3}$	$2.86 \times 10^{-3}$
			A9	40.0	18.39	6.85	17.33	2.529	$1.42 \times 10^{-3}$	$1.49 \times 10^{-3}$	$1.60 \times 10^{-3}$
			A10	50.0	22.99	6.13	17.34	2.828	$9.50 \times 10^{-4}$	$1.01 \times 10^{-3}$	$1.07 \times 10^{-3}$
1.7	0.3	0.15	B1	2.5	1.33	26.76	4.09	0.153	$2.48 \times 10^{-2}$	$2.15 \times 10^{-2}$	$1.42 \times 10^{-1}$
			B2	3.0	1.59	24.43	6.43	0.263	$2.10 \times 10^{-2}$	$1.97 \times 10^{-2}$	$7.73 \times 10^{-2}$
			B3	4.0	2.12	21.15	9.22	0.436	$1.55 \times 10^{-2}$	$1.59 \times 10^{-2}$	$3.98 \times 10^{-2}$
			B4	6.0	3.19	17.27	12.11	0.701	$9.00 \times 10^{-3}$	$1.01 \times 10^{-2}$	$1.76 \times 10^{-2}$
			B5	8.0	4.25	13.79	13.94	1.011	$6.00 \times 10^{-3}$	$5.50 \times 10^{-3}$	$7.74 \times 10^{-3}$
			B6	10.0	5.31	13.38	15.10	1.129	$3.98 \times 10^{-3}$	$4.35 \times 10^{-3}$	$5.82 \times 10^{-3}$
			B7	15.0	7.97	10.92	17.28	1.582	$1.95 \times 10^{-3}$	$1.83 \times 10^{-3}$	$2.17 \times 10^{-3}$
			B8	20.0	10.63	9.46	17.34	1.833	$1.06 \times 10^{-3}$	$1.18 \times 10^{-3}$	$1.34 \times 10^{-3}$
			B9	30.0	15.94	7.73	18.74	2.425	$4.52 \times 10^{-4}$	$4.75 \times 10^{-4}$	$5.15 \times 10^{-4}$
			B10	40.0	21.26	6.69	19.20	2.870	$2.22 \times 10^{-4}$	$2.64 \times 10^{-4}$	$2.80 \times 10^{-4}$

Saladino et al., 2019). This is illustrated in Fig. 2, which shows the density configuration for simulation A4 in the vicinity of the binary system. For the purposes of studying the accretion process, we focus on the global accretion rates rather than the internal properties of the accretion discs.

Table 1 lists the mass accretion efficiencies obtained from our simulations ( $\eta_{\text{sim}}$ ) alongside the analytical estimates  $\eta_{\text{BHL}}$  and  $\eta_{\text{TT}}$ . Calculating these analytical values requires the dimensionless parameters  $q$  and  $w = v_w/v_o$ . While  $q$  is fixed for each simulation set and  $v_o$  is constant for a given circular orbit, determining  $v_w$  is more complex, as it should correspond to the actual wind velocity encountered by the accretor. Although  $v_w$  is often assumed to match the unperturbed stellar wind velocity ( $v_{w,u}$ ) at the accretor's orbital distance (solid line in Fig. 1), the binary's gravitational potential significantly alters the local flow (see, e.g., Saladino et al., 2019). As evidenced by the symbols in Fig. 1 and further illustrated by the velocity profile in Fig. 3, the effective velocity frequently departs from the unperturbed profile. This discrepancy is most pronounced in compact orbits and slow-wind regimes, with the specific magnitude of these variations depending on the orbital separation and the wind acceleration profile.

To account for this, we directly measure the gas velocity in the vicinity of the accretor from our hydrodynamical simulations. Following the methodology illustrated in Fig. 2, we measure  $v_w$  at the leading intersection between a radial axis from the primary and a circle of radius  $r_{\text{acc}}$  centered on the accretor. Measuring  $v_w$  in the upstream direction is crucial to capture the actual wind velocity encountered by the accretor before the flow is further modified by the bow shock and the accretion disk. This characteristic scale is defined using the unperturbed wind velocity

( $v_{w,u}$ ) as

$$r_{\text{acc}} = \frac{Gm_2}{v_{w,u}^2 + v_o^2}. \quad (10)$$

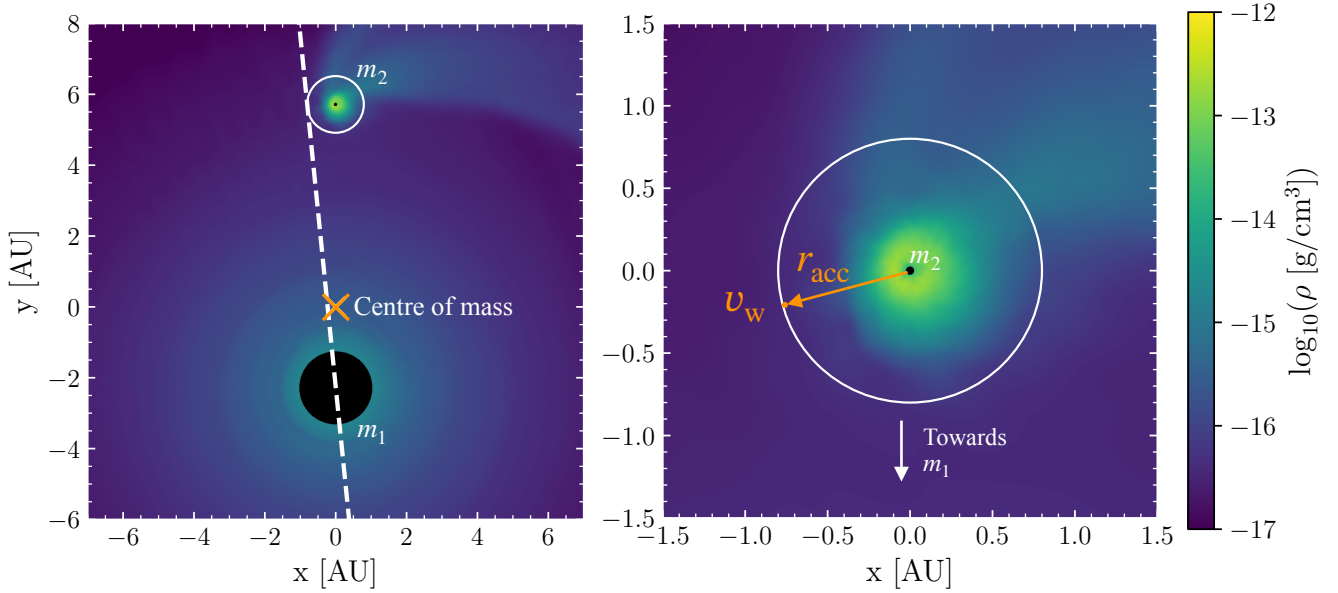
We remark that in all simulations,  $r_{\text{acc}}$  fully encloses the accretion disc as illustrated in Fig. 2.

The results listed in Table 1 are presented in the top panel of Fig. 4. Using the locally measured  $v_w$  provides a physically accurate basis for computing  $w$  and comparing the analytical estimations of the mass accretion efficiencies ( $\eta_{\text{TT}}$  and  $\eta_{\text{BHL}}$ ) against that obtained directly from our numerical results ( $\eta_{\text{sim}}$ ). Our comparison shows that for simulations with  $w > 1$ , all three quantities converge to similar values ( $\eta_{\text{sim}} \approx \eta_{\text{TT}} \approx \eta_{\text{BHL}}$ ), although we invariably find that  $\eta_{\text{TT}} < \eta_{\text{BHL}}$ . However, in the slow-wind regime ( $w < 1$ ), we confirm that the standard BHL prescription systematically overestimates the accretion efficiency, while the geometrically corrected model faithfully reproduces the simulation results. As quantified in the bottom panel of this figure,  $\eta_{\text{TT}}$  exhibits an average error of only 10% (ranging from 3% to 19%), whereas  $\eta_{\text{BHL}}$  deviates by an average error of 100%, with discrepancies escalating up to 500% in certain regimes.

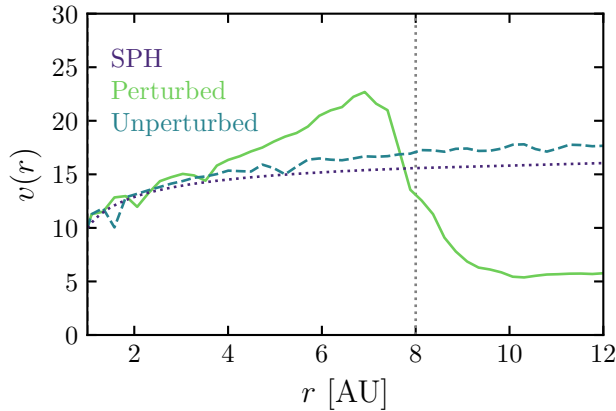
## 5. Discussion

Table 1 and Fig. 4 clearly demonstrate that the mass accretion efficiencies of the analytical predictions of Tejeda & Toalá (2025) closely align with our numerical results. Such agreement confirms that the proposed geometrical correction provides an effective refinement to the standard BHL formalism when applied to binary systems, particularly in the slow-wind regime ( $w < 1$ ).

Our analysis reinforces earlier conclusions of Tejeda & Toalá (2025) that relying on an unperturbed wind profile ( $v_{w,u}$ ) leads



**Figure 2.** Density map for simulation A4 in the orbital plane. **Left:** Global view showing the donor ( $m_1$ ), the accretor ( $m_2$ ), and the system’s center of mass (cross). **Right :** Close-up of the secondary and its associated accretion disk. In both panels, the dashed circle centered on  $m_2$  represents the characteristic radius  $r_{acc}$ , marking the location where the upstream wind velocity ( $v_w$ ) is measured to represent the actual flow conditions encountered by the accretor.



**Figure 3.** Velocity profiles for simulation A4, extracted along the dashed axis shown in the left panel of Fig. 2. The perturbed profile (solid line) represents the velocity measured in the direction toward the secondary, whereas the unperturbed profile (dashed) corresponds to the opposite direction. For comparison, the theoretical wind profile ( $v_{w,u}$ ) from Fig. 1 is shown in a dotted line. The vertical dotted line indicates the orbital separation  $a = 8$  AU.

to inaccurate estimates of the mass accretion rate. Instead, the appropriate velocity to employ is the local gas velocity measured in the upstream direction in the immediate vicinity of the accretor ( $v_w$ ), which faithfully represents the conditions experienced by the accreting object.

The inaccuracy of using  $v_{w,u}$  stems from the fact that the presence of the accretor and its gravitational potential significantly perturb the local gas velocity field. To illustrate this effect, Fig. 3 shows the velocity profile extracted along the radial axis shown in Fig. 2 for simulation A4. The profile measured toward the accretor departs markedly from the expected wind solution, with the gas

velocity effectively slowing down as it approaches the secondary. In contrast, the velocity profile extracted in the direction away from the accretor closely follows the unperturbed wind profile predicted by PHANTOM.

To further investigate these discrepancies, Fig. 5 presents the fractional difference between the local gas velocity experienced by the accretor and the value expected from the unperturbed wind profile, defined as  $1 - v_{w,u}/v_w$ . The largest deviations occur in simulations with orbital separations  $a \leq 10$  AU, which correspond to the region where most of the wind acceleration takes place in our PHANTOM models.

A complementary analysis is shown in Fig. 6, where we evaluate the accuracy of the  $\eta_{TT}$  prescription using three different velocity inputs: the upstream local velocity  $v_w$  (top panel), the unperturbed wind velocity  $v_{w,u}$  (middle panel), and the terminal wind velocity  $v_\infty$  (bottom panel). The top panel provides an alternative representation of Fig. 4-bottom, confirming that adopting the local wind velocity near the accretor reproduces the simulated accretion efficiencies with high fidelity. In contrast, relying on the unperturbed wind velocity (middle panel) introduces errors of  $\sim 50\%$  for compact orbits and up to  $\sim 80\%$  for the widest configurations in Family B. Nevertheless, these discrepancies remain significantly smaller than those produced by the standard BHL formulation.

In practice, observers rarely have access to the perturbed local flow near the accretor, relying instead on estimates of the donor’s terminal wind velocity,  $v_\infty$ . The bottom panel of Fig. 6 shows that combining  $v_\infty$  with the  $\eta_{TT}$  model yields acceptable uncertainties, typically within  $\approx 50\%$  for the inferred mass accretion efficiency. This suggests that the geometrical correction remains a robust tool even when local flow details are unresolved.

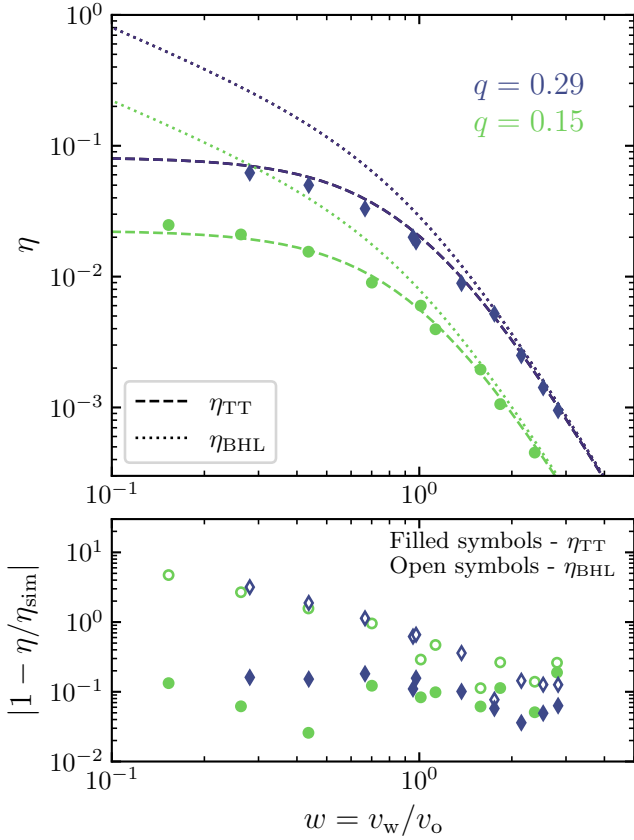


**Figure 4. Top:** Mass accretion efficiency  $\eta$  as a function of the wind dimensionless parameter  $w$ . Analytical predictions from the geometrically corrected model ( $\eta_{\text{TT}}$ , dashed line) and the standard BHL implementation ( $\eta_{\text{BHL}}$ , dotted line) are shown for comparison. **Bottom:** Fractional errors between the analytical predictions and the numerical results. In both panels, diamonds and bullets represent measurements from the A1–A10 ( $q = 2.86$ ) and B1–B10 ( $q = 0.15$ ) simulation families, respectively.

### 5.1. Comparison with previous works

We acknowledge the substantial body of high-quality research addressing accretion in binary systems within the slow-wind regime (e.g., de Val-Borro et al., 2009; Theuns et al., 1996; Lee et al., 2022; Liu et al., 2017; Malfait et al., 2024; Nagae et al., 2004; Saladino et al., 2019, and references therein). Typically, these studies compare numerically-derived accretion efficiencies against predictions from the standard BHL formulation, consistently reporting significant discrepancies. We identify two primary reasons for these departures.

First, many adapted BHL prescriptions lack a complete physical motivation, often introducing an *ad hoc* efficiency parameter,  $\alpha_{\text{BHL}}$ , to reconcile simulations with analytical expectations (see Section 1). In contrast, the  $\eta_{\text{TT}}$  model accounts for the inherent tilt of the accretion cylinder caused by the relative orbital motion of the binary. This geometric correction naturally reduces the effective accretion cross-section, allowing the model to recover simulated results across all wind regimes without empirical tuning.

Second, several studies compute mass accretion efficiencies using wind velocities derived from unperturbed, single-star wind profiles. As demonstrated in our analysis, this approach neglects

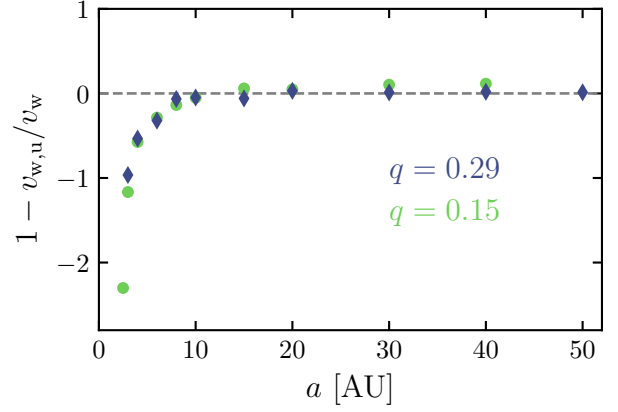


**Figure 5.** Fractional difference between the unperturbed wind velocity ( $v_{w,u}$ ) and the local gas velocity measured from the simulations ( $v_w$ ), defined as  $1 - v_{w,u}/v_w$ . Symbols represent results for both simulation families (A and B) as a function of orbital separation.

the strong dynamical influence of the accretor, which perturbs the local wind velocity experienced by the accreting object. This effect is most pronounced at the small orbital separations explored here ( $a < 10$  AU).

### 5.2. On Symbiotic Systems

Improving our understanding of the wind accretion mechanism in the slow-wind regime has a direct impact on the interpretation of observed symbiotic systems, where a WD accretes from the wind of a RG or AGB star. These late-type stars typically exhibit stellar wind velocities of  $v_w = 5\text{--}20$  km s $^{-1}$  (e.g., Ramstedt et al., 2020; Wallström et al., 2025) and orbital velocities of  $v_o = 30\text{--}50$  km s $^{-1}$ . Consequently, symbiotic systems have typical  $w$  values below 1.

The SPH simulations presented here are intended to broadly encompass the observed properties of known symbiotic systems. For example, Fig. 7 illustrates the parameter space occupied by the two families of simulations within a  $q - w$  diagram. The figure includes contours of constant  $\log_{10}(\eta)$  values alongside the positions of observed symbiotic systems (see Appendix A for details on the data sources). In general, the observations and simulations occupy a similar region in the  $q - w$  diagram, spanning efficiencies between the  $\log_{10}(\eta) = -4$  and  $-1$ .

The accretion luminosity in a symbiotic system can be estimated as

$$L_{\text{acc}} = \frac{1}{2} \frac{G m_{\text{WD}}}{R_{\text{WD}}} \dot{M}_{\text{acc}}, \quad (11)$$

where  $m_{\text{WD}}$  and  $R_{\text{WD}}$  are the mass and radius of the accreting WD, respectively, and  $\dot{M}_{\text{acc}} = \eta_{\text{sim}} \dot{M}_w$  is the mass accretion rate. Adopting a typical radius of  $R_{\text{WD}} = 0.01 R_{\odot}$  (e.g., Boshkayev et al., 2016; Pasquini et al., 2023; Karinkuzhi et al., 2024) and using the accretor masses from our simulations, we estimate accretion luminosities in the range of  $L_{\text{acc}} = [0.04 - 23] \times 10^{33}$  erg s $^{-1} = [0.01 - 6] L_{\odot}$ . These values are consistent with the X-ray luminosities reported for symbiotic systems (see, e.g., Guerrero et al., 2024, and references therein).

## 6. Summary

In this work, we have presented a suite of SPH simulations designed to test wind accretion in binary systems operating in the slow-wind regime ( $w < 1$ ). Our primary goal was to assess the validity of analytical prescriptions for the mass accretion efficiency

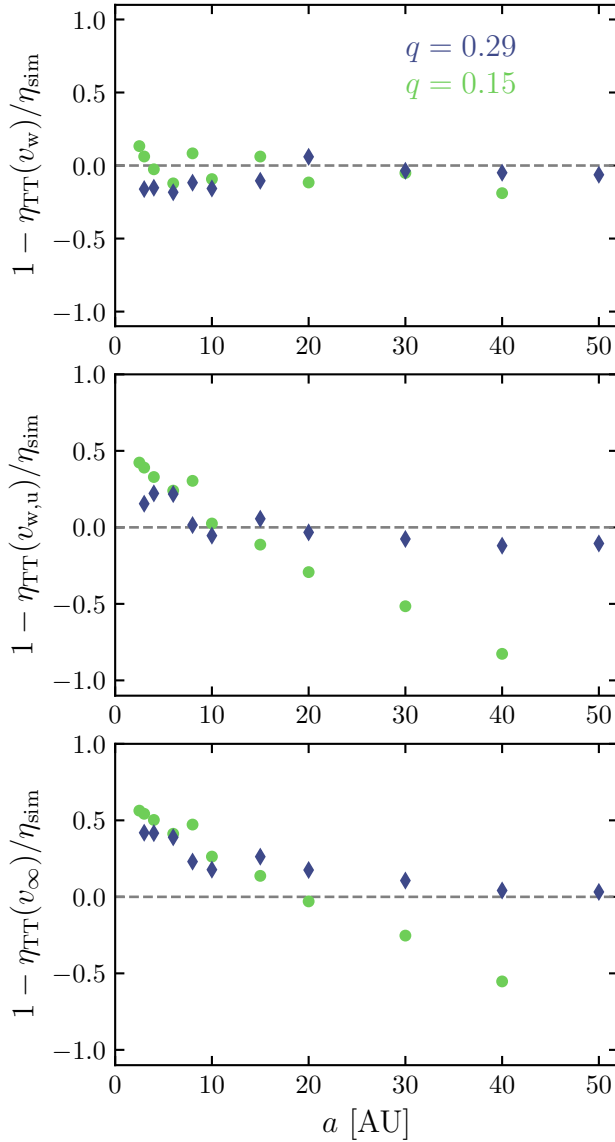


**Figure 6.** Accuracy of the  $\eta_{\text{TT}}$  analytical prescription using different velocity estimates relative to the simulated efficiency ( $\eta_{\text{sim}}$ ). The panels show the fractional error ( $1 - \eta_{\text{TT}}/\eta_{\text{sim}}$ ) using: the local upstream velocity ( $v_w$ , top), the unperturbed wind velocity ( $v_{w,u}$ , middle), and the terminal wind velocity ( $v_\infty$ , bottom). Symbols represent results for both simulation families as a function of orbital separation.

by directly comparing numerical results with both the standard implementation of the BHL formalism and the geometrically corrected model proposed by [Tejeda & Toalá \(2025\)](#).

We explored accretion in circular binary configurations and demonstrated that the standard BHL implementation systematically overestimates the mass accretion efficiency in the slow-wind regime ( $w < 1$ ). In contrast, the  $\eta_{\text{TT}}$  formulation reproduces the accretion efficiencies measured directly from the simulations remarkably well across the full range of explored parameters. A fundamental aspect of this agreement is the geometric foundation of the model: as the accretor orbits the donor star, the accretion cylinder is not aligned with the radial wind flow but is instead tilted by the relative orbital motion. This wind aberration effectively reduces the accretion cross-

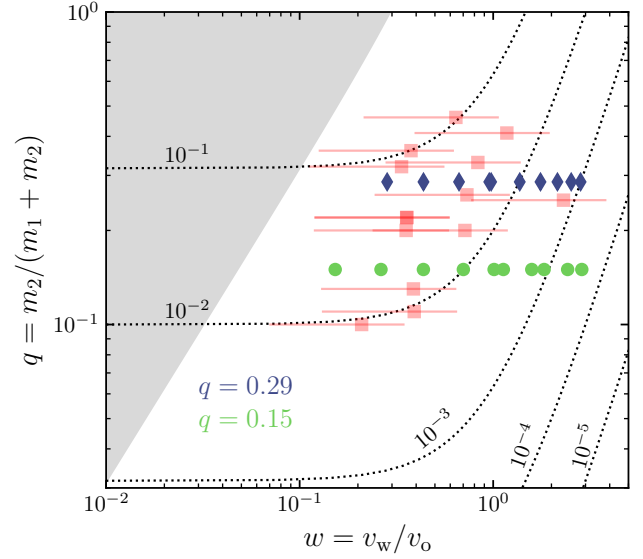


**Figure 7.** Parameter space of mass accretion efficiency in the  $q$ - $w$  plane. Symbols represent the two simulation families (A and B), while dashed lines indicate contours of constant  $\log_{10}(\eta_{\text{TT}})$ . The square symbols with error bars denote the properties of observed symbiotic systems (see Table A1). The shaded region at high  $q$  and low  $w$  represents the portion of the parameter space where the analytical model of [Tejeda & Toalá \(2025\)](#) is formally invalid due to the breakdown of the underlying geometric assumptions.

section, a physical correction that is naturally captured by the  $\eta_{\text{TT}}$  prescription. Consequently, the model recovers the measured efficiencies across all wind regimes without the need for empirical efficiency factors often required in traditional BHL implementations.

A key result of this study is that the relevant wind velocity for accretion estimates is not the value derived from the unperturbed wind profile ( $v_{w,u}$ ), but rather the local gas velocity measured upstream in the vicinity of the accretor ( $v_w$ ). Our simulations show that the gravitational potential of the accretor significantly perturbs the wind flow, modifying the effective relative velocity. This effect is especially pronounced within the wind acceleration zone of the primary star. While using the locally measured velocity is essential for achieving formal agreement between analytical predictions and numerical results, we note that for observed systems, adopting the terminal wind velocity typically yields errors of  $\lesssim 50\%$ . Crucially, this discrepancy remains significantly smaller than the order-of-magnitude errors produced by the standard BHL implementation in the slow-wind regime.

Furthermore, our numerical results provide a robust benchmark for the wind accretion approximation developed by [Tejeda & Toalá \(2025\)](#). As this prescription has already been applied by [Maldonado et al. \(2025a,b\)](#) to study the long-term evolution of accreting white dwarfs in binary systems, our work provides the necessary hydrodynamical validation for those studies.

Overall, our results provide strong numerical support for the geometrically corrected wind accretion model, especially in the slow-wind regime. This provides a physically motivated framework for modeling wind-fed accretion in a wide variety of binary systems, ranging from symbiotic stars to other interacting binaries with evolved donors.

## ■ REFERENCES

- Boffin, H. M. J. 2015, in *Astrophysics and Space Science Library*, Vol. 413, *Astrophysics and Space Science Library*, ed. H. M. J. Boffin, G. Carraro, & G. Beccari, 153, doi: [10.1007/978-3-662-44434-4\\_7](https://doi.org/10.1007/978-3-662-44434-4_7)
- Bondi, H., & Hoyle, F. 1944, *MNRAS*, 104, 273, doi: [10.1093/mnras/104.5.273](https://doi.org/10.1093/mnras/104.5.273)
- Boshkayev, K. A., Rueda, J. A., Zhami, B. A., Kalymova, Z. A., & Balgymbekov, G. S. 2016, in *International Journal of Modern Physics Conference Series*, Vol. 41, *International Journal of Modern Physics Conference Series*, 1660129, doi: [10.1142/S2010194516601290](https://doi.org/10.1142/S2010194516601290)
- Davidson, K., & Ostriker, J. P. 1973, *ApJ*, 179, 585, doi: [10.1086/151897](https://doi.org/10.1086/151897)
- de Val-Borro, M., Karovska, M., & Sasselov, D. 2009, *ApJ*, 700, 1148, doi: [10.1088/0004-637X/700/2/1148](https://doi.org/10.1088/0004-637X/700/2/1148)
- Guerrero, M. A., Montez, R., Ortiz, R., Toalá, J. A., & Kastner, J. H. 2024, *A&A*, 689, A62, doi: [10.1051/0004-6361/202450155](https://doi.org/10.1051/0004-6361/202450155)
- Hainich, R., Oskinova, L. M., Torrejón, J. M., et al. 2020, *A&A*, 634, A49, doi: [10.1051/0004-6361/201935498](https://doi.org/10.1051/0004-6361/201935498)
- Hoyle, F., & Lyttleton, R. A. 1939, *Proceedings of the Cambridge Philosophical Society*, 35, 405, doi: [10.1017/S0305004100021150](https://doi.org/10.1017/S0305004100021150)
- Huarte-Espinosa, M., Carroll-Nellenback, J., Nordhaus, J., Frank, A., & Blackman, E. G. 2013, *MNRAS*, 433, 295, doi: [10.1093/mnras/stt725](https://doi.org/10.1093/mnras/stt725)
- Karinkuzhi, D., Mukhopadhyay, B., Wickramasinghe, D., & Tout, C. A. 2024, *MNRAS*, 529, 4577, doi: [10.1093/mnras/stae829](https://doi.org/10.1093/mnras/stae829)
- Lee, Y.-M., Kim, H., & Lee, H.-W. 2022, *ApJ*, 931, 142, doi: [10.3847/1538-4357/ac67d6](https://doi.org/10.3847/1538-4357/ac67d6)
- Liu, Z.-W., Stancliffe, R. J., Abate, C., & Matroziis, E. 2017, *ApJ*, 846, 117, doi: [10.3847/1538-4357/aa8622](https://doi.org/10.3847/1538-4357/aa8622)
- Maldonado, R. F., Toalá, J. A., Rodríguez-González, J. B., & Tejada, E. 2025a, *ApJ*, 989, 108, doi: [10.3847/1538-4357/ade9a5](https://doi.org/10.3847/1538-4357/ade9a5)
- Maldonado, R. F., Toalá, J. A., Tejada, E., & Rodríguez-González, J. B. 2025b, *MNRAS*, 544, 2387, doi: [10.1093/mnras/staf1773](https://doi.org/10.1093/mnras/staf1773)
- Malfait, J., Siess, L., Esseldeurs, M., et al. 2024, *A&A*, 691, A84, doi: [10.1051/0004-6361/202450338](https://doi.org/10.1051/0004-6361/202450338)
- Merc, J. 2025, *Galaxies*, 13, 49, doi: [10.3390/galaxies13030049](https://doi.org/10.3390/galaxies13030049)
- Merc, J., Gális, R., & Wolf, M. 2019, *Research Notes of the American Astronomical Society*, 3, 28, doi: [10.3847/2515-5172/ab0429](https://doi.org/10.3847/2515-5172/ab0429)
- Mikołajewska, J. 2003, in *Astronomical Society of the Pacific Conference Series*, Vol. 303, *Symbiotic Stars Probing Stellar Evolution*, ed. R. L. M. Corradi, J. Mikołajewska, & T. J. Mahoney, 9, doi: [10.48550/arXiv.astro-ph/0210489](https://doi.org/10.48550/arXiv.astro-ph/0210489)
- Millar, T. J. 2004, in *Asymptotic Giant Branch Stars*, ed. H. J. Habing & H. Olofsson, 247–289, doi: [10.1007/978-1-4757-3876-6\\_5](https://doi.org/10.1007/978-1-4757-3876-6_5)
- Mohamed, S., & Podsiadlowski, P. 2007, in *Astronomical Society of the Pacific Conference Series*, Vol. 372, *15th European Workshop on White Dwarfs*, ed. R. Napiwotzki & M. R. Burleigh, 397
- Mohamed, S., & Podsiadlowski, P. 2012, *Baltic Astronomy*, 21, 88, doi: [10.1515/astro-2017-0362](https://doi.org/10.1515/astro-2017-0362)
- Nagae, T., Oka, K., Matsuda, T., et al. 2004, *A&A*, 419, 335, doi: [10.1051/0004-6361:20040070](https://doi.org/10.1051/0004-6361:20040070)
- Pasquini, L., Pala, A. F., Salaris, M., et al. 2023, *MNRAS*, 522, 3710, doi: [10.1093/mnras/stad1252](https://doi.org/10.1093/mnras/stad1252)
- Podsiadlowski, P., & Mohamed, S. 2007, *Baltic Astronomy*, 16, 26
- Price, D. J., Wurster, J., Tricco, T. S., et al. 2018, *PASA*, 35, e031, doi: [10.1017/pasa.2018.25](https://doi.org/10.1017/pasa.2018.25)
- Ramstedt, S., Vlemmings, W. H. T., Doan, L., et al. 2020, *A&A*, 640, A133, doi: [10.1051/0004-6361/201936874](https://doi.org/10.1051/0004-6361/201936874)
- Saladino, M. I., & Pols, O. R. 2019, *A&A*, 629, A103, doi: [10.1051/0004-6361/201935625](https://doi.org/10.1051/0004-6361/201935625)
- Saladino, M. I., Pols, O. R., & Abate, C. 2019, *A&A*, 626, A68, doi: [10.1051/0004-6361/201834598](https://doi.org/10.1051/0004-6361/201834598)
- Shakura, N. I., Postnov, K. A., Kochetkova, A. Y., et al. 2015, *Astronomy Reports*, 59, 645, doi: [10.1134/S1063772915070112](https://doi.org/10.1134/S1063772915070112)
- Siess, L., Homan, W., Toupin, S., & Price, D. J. 2022, *A&A*, 667, A75, doi: [10.1051/0004-6361/202243540](https://doi.org/10.1051/0004-6361/202243540)
- Spitzer, L. 1978, *Physical processes in the interstellar medium*, doi: [10.1002/9783527617722](https://doi.org/10.1002/9783527617722)
- Tejada, E., & Toalá, J. A. 2025, *ApJ*, 980, 226, doi: [10.3847/1538-4357/ada953](https://doi.org/10.3847/1538-4357/ada953)
- Theuns, T., Boffin, H. M. J., & Jorissen, A. 1996, *MNRAS*, 280, 1264, doi: [10.1093/mnras/280.4.1264](https://doi.org/10.1093/mnras/280.4.1264)
- Vasquez-Torres, D. A., Toalá, J. A., Sacchi, A., et al. 2024, *MNRAS*, 535, 2724, doi: [10.1093/mnras/stae2538](https://doi.org/10.1093/mnras/stae2538)
- Vathachira, I. B., Hillman, Y., & Kashi, A. 2026, *ApJ*, 997, 278, doi: [10.3847/1538-4357/ae27c7](https://doi.org/10.3847/1538-4357/ae27c7)
- Wallström, S. H. J., Scicluna, P., Srinivasan, S., et al. 2025, *A&A*, 704, A276, doi: [10.1051/0004-6361/202556298](https://doi.org/10.1051/0004-6361/202556298)
- Weng, S.-S., & Ji, L. 2024, *Universe*, 10, 453, doi: [10.3390/universe10120453](https://doi.org/10.3390/universe10120453)

## 7. ACKNOWLEDGEMENTS

JAT and DAVT thank support from UNAM DGAPA PAIIT project IN102324. This work has made an extensive use of NASA's Astrophysics Data System (ADS).

## ■ APPENDICES

### A. Observed Symbiotic Systems

Table A1 lists the properties of various symbiotic systems retrieved from the *New Online Database of Symbiotic Variables<sup>2</sup>* (Merc et al., 2019). This table includes the object name, the masses of the stellar components ( $m_1$  and  $m_2$ ), the binary period ( $T$ ), the estimated orbital separation ( $a$ ), and the orbital velocity ( $v_o$ ). Furthermore, it provides the dimensionless mass ratio  $q$ , the dimensionless velocity parameter  $w$ , the estimated mass accretion efficiency  $\eta_{\text{TT}}$  obtained from Equation (6), the Roche Lobe radius ( $R_{\text{RL}}$ ), and the radius of the late-type companion ( $R_{\text{RC}}$ ).

For our analysis, we only selected symbiotic systems where the estimated Roche Lobe radius is at least three times larger than the radius of the late-type component ( $R_{\text{RL}} \geq 3 R_{\text{RC}}$ ). This criterion ensures that the systems are operating within the wind-accretion regime rather than being dominated by Wind Roche Lobe Overflow. We note that a similar selection condition was adopted by Maldonado et al. (2025a); consequently, the objects listed in Table A1 are the same as those analyzed in that work.

<sup>2</sup><https://sirrah.troja.mff.cuni.cz/~merc/nodsv/>

**Table A1.** Binary and orbital parameters estimated for symbiotic systems. The columns list the mass of the primary (donor)  $m_1$ , mass of the secondary (accretor)  $m_2$ , orbital separation  $a$ , orbital velocity  $v_o$ , orbital period  $T$ , dimensionless mass ratio  $q = m_2/(m_1 + m_2)$ , dimensionless velocity parameter  $w = v_w/v_o$ , mass accretion efficiencies  $\eta_{\text{TT}}$ , Roche Lobe radius  $R_{\text{LB}}$  and the red giant radius  $R_{\text{RG}}$ . We assume a typical wind velocity of  $v_w = 12 \pm 8 \text{ km s}^{-1}$ .

Object	$m_1$ [ $M_{\odot}$ ]	$m_2$ [ $M_{\odot}$ ]	$T$ [yr]	$a$ (AU)	$v_o$ [ $\text{km s}^{-1}$ ]	$q$	$w$	$\eta_{\text{TT}}$	$R_{\text{RL}}$ [AU]	$R_{\text{RG}}$ [AU]
<i>o</i> Cet	2.00	0.65	497.90	87.3	5.2	0.25	1.35	$7.6 \times 10^{-3}$	42.1	1.9
AG Dra	1.20	0.50	1.51	1.6	31.1	0.29	0.48	$5.6 \times 10^{-2}$	0.7	0.16
AG Peg	2.60	0.65	2.23	2.5	33.8	0.20	0.44	$2.8 \times 10^{-2}$	1.3	0.4
BX Mon	3.70	0.55	3.78	3.9	31.0	0.13	0.48	$1.1 \times 10^{-2}$	2.2	0.7
CH Cyg	2.20	0.56	15.58	8.8	16.8	0.20	0.89	$1.2 \times 10^{-2}$	4.4	1.3
EG And	1.46	0.40	1.32	1.5	33.5	0.22	0.45	$3.3 \times 10^{-2}$	0.7	0.6
ER Del	3.00	0.70	5.72	5.0	25.8	0.19	0.58	$2.0 \times 10^{-2}$	2.5	0.5
HD 330036	4.46	0.54	4.59	4.8	30.7	0.11	0.49	$7.6 \times 10^{-3}$	2.7	0.1
IV Vir	0.90	0.42	0.77	0.9	35.7	0.32	0.42	$7.3 \times 10^{-2}$	0.4	0.1
LT Del	1.00	0.57	1.24	1.4	31.9	0.36	0.47	$8.8 \times 10^{-2}$	0.6	0.14
PU Vul	1.00	0.50	13.42	6.5	14.4	0.33	1.04	$2.5 \times 10^{-2}$	2.9	0.9
R Aqr	1.00	0.70	42.40	14.6	10.2	0.41	1.47	$1.7 \times 10^{-2}$	6.0	1.4
St 2-22	2.80	0.80	2.51	2.9	33.6	0.22	0.45	$3.4 \times 10^{-2}$	1.4	0.4
TX CVn	3.50	0.40	0.55	1.1	57.4	0.10	0.26	$8.8 \times 10^{-3}$	0.6	0.1
V471 Per	2.30	0.80	17.00	9.4	16.4	0.26	0.92	$1.9 \times 10^{-2}$	4.6	0.05
V934 Her	1.60	1.35	12.02	7.6	18.7	0.46	0.80	$7.7 \times 10^{-2}$	3.0	0.4